

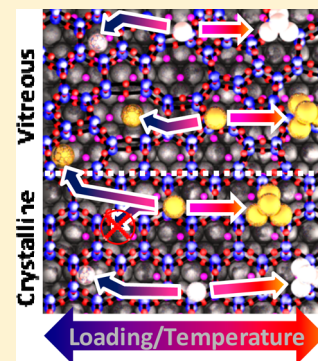
Adsorption of Au and Pd on Ruthenium-Supported Bilayer Silica

Christin Büchner,[†] Leonid Lichtenstein,^{†,§} Stefanie Stuckenholtz,[†] Markus Heyde,^{*,†} Franziska Ringleb,^{†,||} Martin Sterrer,[†] William E. Kaden,^{*,†} Livia Giordano,[‡] Gianfranco Pacchioni,[‡] and Hans-Joachim Freund[†]

[†]Department of Chemical Physics, Fritz Haber Institute of the Max Planck Society, Faradayweg 4-6, D-14195 Berlin, Germany

[‡]Dipartimento di Scienza dei Materiali, Università di Milano-Bicocca, Via Cozzi 53, I-20125 Milano, Italy

ABSTRACT: Adsorption of Au and Pd over bilayer SiO₂/Ru has been investigated using scanning-probe microscopy, X-ray photoemission spectroscopy (XPS), and density functional theory (DFT). Low temperature (~5 K) atomic force microscopy (AFM) and scanning tunneling microscopy (STM) measurements reveal the presence of small adsorption features after exposing the samples to small doses of either metal. In the case of Pd, we note a homogeneous distribution of adsorbates across the entire surface, which consists of both amorphous and crystalline phases. Au, however, adsorbs only over amorphous areas and domain boundaries, which possess larger pores than can be found in the ordered portions of the film. DFT calculations reveal that this difference is rooted in the pore-size-dependent barriers for diffusion of the two metals into the film, where they can then bind stably at the Ru interface. Auger parameter analysis of the Pd 3d and Au 4f core-levels from atoms binding in this manner show upward orbital-energy shifts, which, according to the results of theoretical calculations, originate from effects similar to those causing surface core-level-shifts for such metals. Further analysis of the computational results shows that such atoms donate electron density to the Ru support, which is consistent with XPS results that show band-bending effects related to decreases in the work-function of the sample after adsorbing either metal. Additional features in the XPS studies suggest that a secondary binding mechanism, mediated by cluster formation over the SiO₂ film, becomes increasingly favorable as temperature and loading increase.



1. INTRODUCTION

SiO₂-based materials have a large number of industrial and scientific applications, such as microelectronics and energy conversion technologies.¹ Within the catalysis community, silicates and zeolites are often used as high surface-area supports for activated systems, where tailored porous networks may interact with and stabilize reactive sites while simultaneously influencing selectivity by discriminating against the diffusion or formation of various species within molecular-sieve-like channels.^{2,3} To gain a better understanding of the fundamental properties governing the chemistry within such frameworks, significant effort has been put into developing simplified models of these systems via epitaxial growth of well-defined thin-films over ordered metal surfaces.^{1,4} The advantage of working with such samples is their simplicity and amenability to a wide range of well-developed surface-science techniques, which often require the use of flat and electrically conductive materials.

The first known example of a crystalline, metal-supported silica film was monolayer SiO_{2,5}/Mo(112),⁴ which consists of a hexagonal network of corner-sharing SiO₄ tetrahedra, with each unit binding directly to Mo via Si–O–Mo vertical linkages.^{5,6} Comparative studies of the low-temperature adsorption behavior of several metals over this support showed significant variation, such that some atoms, like Pd, could, while others, like Au, could not penetrate the pores inherent within the film to form stable bonds with the underlying metal substrate.⁷ Subsequent studies revealed that metal-dependent variations in the activation barrier for entry into the hexagonal silica rings

simply reflected differences in the electronic structure of the atoms investigated.⁸ Put more explicitly, the likelihood for atomic diffusion into the pores was shown to be inversely correlated with the degree of occupancy within the valence-level s-orbitals of the metal atoms, which repel filled states within the oxide. In the case of gold, where film penetration is not possible, adsorption occurs solely at antiphase domain boundaries, which contain larger pores than those available elsewhere on the support.

During the time since the initial studies, several new silicate structures have been developed over various metal supports,^{9–11} with bilayer SiO₂/Ru(0001) receiving the most attention. Like the monolayer version, this film also consists of a repeating network of hexagonal rings, but in the newer case, each ring possesses 12 corner sharing SiO₄ tetrahedra, with 6 from each terminus binding through shared Si–O–Si vertical linkages to form a fully saturated bilayer. Unlike the monolayer version, this film does not form covalent bonds to the underlying metal, but is, instead, only weakly physisorbed to the surface. Furthermore, the bilayer version may exhibit crystalline and/or amorphous lateral order depending on the preparation conditions employed.^{12,13} A recent atomically resolved scanning tunneling microscopy (STM)¹² investigation of structures within vitreous regions revealed a network of bilayer rings that was 2-dimensionally consistent with the

Received: June 4, 2014

Revised: August 14, 2014

Published: August 15, 2014

random network theory, which was first postulated by Zachariassen in 1932,¹⁴ and more recently confirmed with X-ray and neutron diffraction results from bulk samples.^{15,16}

Relative to its predecessor, the bilayer film offers a host of new possibilities in terms of metal adsorption. Given its cage-like structure and weak coupling to the support, we must now consider the prospect of binding within the silicate. Furthermore, exploration of the vitreous areas might provide better insights into the various interactions governing adsorption processes in bulk materials, where long-range structural order is unexpected. Of particular interest will be developing a better understanding of how variations in pore size might act to influence the adsorption mechanism(s) of different metal atoms, relative to the process(es) over the monolayer film. To investigate these possibilities, we have conducted the following low-temperature study of Pd and Au atoms deposited over mixed-phase bilayer films using scanning-probe and photoemission techniques in tandem with theory to investigate the structures, locations, binding mechanisms, and resultant electronic properties of the supported metals.

2. EXPERIMENTAL AND THEORETICAL METHODS

2.1. Experimental Details. The experimental portions of this work were conducted within two ultrahigh vacuum (UHV) chambers; one for low-temperature (5 K) scanning-probe microscopy, and the other for X-ray photoemission spectroscopy (XPS). In both cases, bilayer sheets of silica were grown over Ru(0001) supports, which were first cleaned via several cycles of Ar⁺ sputtering and UHV annealing. Creation of well-characterized SiO₂ structures was achieved by evaporating $\sim 1.6 \times 10^{15}$ atoms/cm² Si onto preoxidized 3O-(2 × 2)/Ru(0001) at $T \leq 300$ K, then heating to $T \approx 1200$ K in the presence of 2×10^{-6} mbar O₂, and finally cooling within the oxygen environment. As discussed in previous works, both cooling rate and Si coverage can play a role in determining the overall crystallinity of the film,^{12,13} and the samples discussed herein always exhibited a combination of both 2-dimensionally amorphous and crystalline phases. For brevity, the thin-film system is frequently called SiO₂/Ru, which describes the bilayer film on the oxidized 3O-(2 × 2)/Ru(0001) surface (if not described otherwise, e.g., oxygen-deficient).

In the first setup, films were characterized by low energy electron diffraction (LEED) and Auger electron spectroscopy (AES, combined four-grid optics from Specs) before transfer into the imaging chamber, which is a custom-built, dual-mode STM and noncontact atomic force microscope (nc-AFM). After characterization of the pristine film, small amounts of Pd or Au were deposited onto the SiO₂/3O-(2 × 2)/Ru at ~ 5 K using two custom-built microevaporators positioned within the microscope.¹⁷

In the second setup, film growth was characterized by a combination of LEED (Specs), XPS (Al K α , Specs), and low-energy helium ion scattering spectroscopy (ISS, dual-mode hemispherical analyzer from Specs) in a manner similar to that described elsewhere.¹³ After film growth, controlled amounts of Pd or Au were evaporated onto the sample at ~ 150 K, which was the lowest temperature readily attainable at that time. For the Auger parameter analysis described below, we have made use of Bremsstrahlung radiation from our nonmonochromatic X-ray source to excite transitions requiring photon energies beyond that nominally supplied by our K α transition. Absolute metal concentrations were obtained by direct comparison of Au and Pd intensities with those obtained from Au(111) and

Pd(111) single-crystals. To determine the effective sampling density probed in the reference materials, we employed NIST effective attenuation length calculations to account for the cumulative attenuation effects expected over a depth of 10 nm, beyond which significant quantities of electrons are not expected to escape.¹⁸ The concentrations obtained in this manner showed reasonable agreement ($\pm 10\%$) with values predicted from quartz microbalance measurements made prior to deposition.

2.2. Computational Details. Density functional theory calculations were carried out with a periodic approach and plane wave basis set, as implemented in the VASP code.^{19,20} We explicitly treated four valence electrons for Si ($3s^2 3p^2$), six for O ($2s^2 2p^4$), eight for Ru ($4d^7 5s^1$), ten for Pd ($4d^{10}$), and 11 for Au ($5d^{10} 6s^1$). Core electrons were described with the Projector Augmented Wave (PAW) method,²¹ and the plane wave cutoff was set to 400 eV. The gradient-corrected PBE functional has been employed,²² and we have included an estimate of the van der Waals (VdW) interactions using the pairwise force field implemented in the DFT-D2 method proposed by Grimme.²³ While the R_0 and C_6 values for Si, O, Ru, and Pd were taken from Grimme's paper, $C_6 = 40.62$ J nm⁶ mol⁻¹ and $R_0 = 1.772$ Å were used for Au.²⁴

Crystalline SiO₂ has been modeled by considering the hexagonal bilayer adsorbed on the oxygen covered Ru(0001) surface (3O-(2 × 2)/Ru(0001) structure), as in ref 25. The metal surface was modeled by a five-layer-thick slab at the optimized bulk Ru lattice parameters ($a = 2.73$ Å and $c/a = 1.575$, which compares well with the experimentally derived values of $a = 2.696$ Å and $c/a = 1.582$).²⁶ The slabs were separated by 12 Å of vacuum, and a dipole correction has been added in order to eliminate the interaction between repeated replica. For the adsorption of isolated metal atoms, a (2 × 2) SiO₂ supercell was employed, corresponding to a (4 × 4) Ru(0001) supercell. A (3 × 3 × 1) Monkhorst–Pack grid was used for this supercell, and the positions of the adatom, SiO₂, and the three upper Ru layers were relaxed until the forces were smaller than 0.01 eV/Å³.

To explore the influence of various ring sizes within the amorphous phase of the film, we have made use of unsupported cluster models. For each ring size ($n = 4-8$), the model contains up to the second neighbors of the ring-bordering Si atoms and is terminated by =SiH₂ groups. The resulting n -membered clusters of Si_{4n}O_{6n}H_{4n} composition have been surrounded by at least 12 Å of vacuum in each direction, and only the Γ -point was considered for reciprocal space integration. A complete relaxation was performed for each cluster prior to metal adsorption, and starting from this configuration, only the ring atoms, their first neighbors, and the additional metal atoms were allowed to relax when determining the optimal structural configurations of the adsorbate-containing systems.

In all cases, we have made use of the well-established dimer method to evaluate the barriers toward metal incorporation into the pores of the silica models investigated.²⁷ Furthermore, atomic charges of the metal-incorporated models have been obtained within the scheme of charge density decomposition proposed by Bader,²⁸ while magnetic moments were evaluated from the projection of the spin density into atomic spheres, and the work-function (Φ) was estimated as the difference between the vacuum level and the Fermi energy. We note that the work-function of Ru(0001) computed with gradient corrected functionals (GGA), 4.9 eV, is underestimated with respect to

the experimental value (5.4 eV),²⁹ while local density approximated functional (LDA) calculations give $\Phi = 5.4$ eV, in better agreement with the physically observable value. It is important to note that this is not related to structural effects since we have verified that a GGA calculation on the LDA geometry gives essentially the same results as those from the GGA optimized structure. Since we are more interested in the change of Φ upon metal adsorption than the absolute values in the present work, we have chosen to report Φ s obtained at the GGA level, as this method gives a satisfactory description of the energetics and the other electronic properties.

Core-level electron binding energies have been computed in both initial-state approximation and including final-state effects. In the initial-state calculations, we first established a full self-consistency with the frozen core electrons before solving the Kohn–Sham equations for core electrons inside the PAW sphere. The core-level shift (CLS) between different samples is then computed as the difference of the resulting Kohn–Sham eigenvalues (referred to the Fermi level). In the final-state calculations, excitation of a single core-level electron is accounted for by the corresponding core-excited ionic PAW potential. Because of the frozen core, this method accounts for screening by valence electrons but neglects screening by core electrons. Within this approach, core-level binding energy shifts can be computed as total energy differences.³⁰ For these calculations we have constructed a model with 5 Pd(111) layers added below the SiO₂/3O-(2 × 2)/Ru(0001) slab, so that the isolated adatom and the fully coordinated (bulk) reference Pd are in the same unit cell, allowing for a direct comparison of their core-level binding energies (same internal reference).

3. RESULTS AND DISCUSSION

3.1. Scanning-Probe Microscopy. As alluded to, the silica films in this work were always mixed-phase, with extended patches of both crystalline and amorphous regions. While crystalline areas exhibit a characteristic honeycomb structure, which consists of interlocking networks of hexagonal SiO₂ rings, with 6 surface-bound Si atoms per ring (Figure 1a,c), amorphous areas contain a distribution of SiO₂ rings, which range from 4- to 9-membered in size (Figure 1b,d). Furthermore, a close examination of boundary structures reveals that, while the transition phases between amorphous and crystalline patches necessarily show some heterogeneity,³¹ the domain boundaries within crystalline areas consist almost exclusively of alternating 5- and 8-membered rings (see below).

Following evaporative loading, Au and Pd should initially adsorb as predominantly monomeric species. Given the low deposition temperature (<5 K), we presume that the metal species lack the mobility needed to form large clusters, and indeed, no structures larger than 9 Å were observed. In STM, the adsorbed atoms appear as bright protrusions of different shapes and heights between 0.5 and 1 Å (Figure 2). While the majority of the Pd (Au) protrusions exhibit a butterfly (crescent) shape, we also note the presence of round protrusions, which occur less frequently and result in greater tip retractions when imaging in constant current mode (i.e., appear to extend further from the interface). On the basis of correlations between the different shapes and their lateral positions, relative to the support, we tentatively assign the two features to metal species located at different binding sites (i.e., round features are always centered within the rings, while angled features are always off-center). Additionally, it is worth pointing out that the positions and shapes of these features do

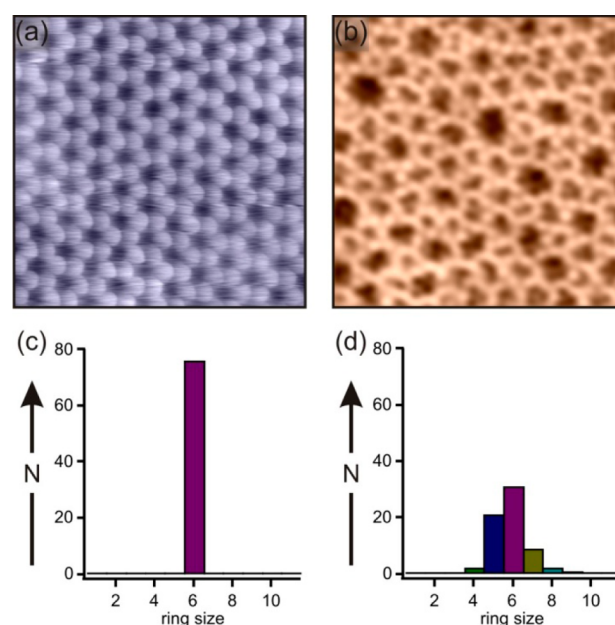


Figure 1. Different domains of the silica film. (a) STM of the crystalline phase, 5×5 nm², $V_s = 3$ V, $I_T = 100$ pA. (b) nc-AFM image of the amorphous phase, 5×5 nm², 100 mV, recorded at constant height. Below: Ring statistics of both images. (c) Crystalline patches consist of only six-membered rings. (d) The amorphous domain shows a distribution of ring sizes, ranging from four to nine (surface) silicon atoms per ring.

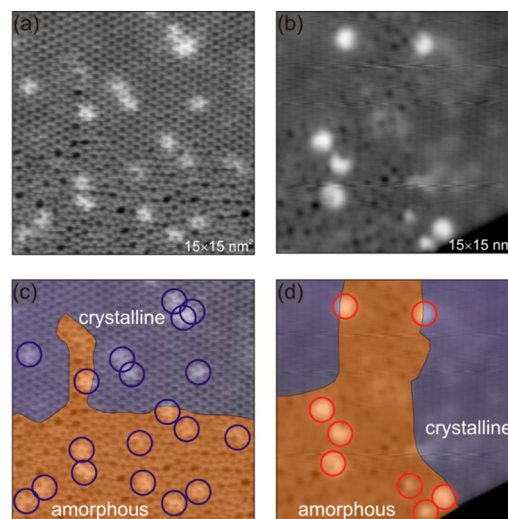


Figure 2. STM images showing Pd and Au adsorption over silica. (a,c) Pd on SiO₂; (b,d) Au on SiO₂. (c,d) Crystalline regions are colored purple and amorphous regions are colored orange. Note: The nonregular dimmer features throughout the crystalline portions of both samples likely result from native SiO₂/Ru species, as they are present both before and after metal adsorption. All images: 15×15 nm², $V_s = 2$ V, $I_T = 100$ pA.

not change significantly over the course of several imaging cycles, which suggests that the adsorbed species are most likely binding below the atomic surface of the film and, as such, remain resistant to tip-induced diffusion effects.

In Figure 2 it is noteworthy that Pd atoms adsorb within both crystalline and amorphous domains of the silica film, whereas Au is only found within the amorphous areas. This finding is expressed quantitatively in Figure 3, which further

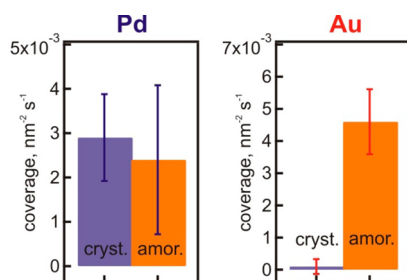


Figure 3. Statistical evaluation of particles adsorbed on bilayer SiO₂. For the Pd and Au coverage statistics, STM images amounting to 3700 and 3000 nm² were evaluated, respectively. Note: In order to compare several different dosages in one figure, we have plotted time-dependent coverages, which have been determined by noting the number of features within an area of the sample following a given amount of time exposing the sample to the microevaporator flux.

suggests that Pd binds to the surface with complete indifference to the SiO₂ phase, while Au adatoms show complete preference for the amorphous structures. Note that while various metal coverages ranging from 0.034 to 0.092 nm⁻² were employed to generate this figure, no systematic variations in the relative site preferences, rate of particle formation, or particle size were observed as a function of dose. This further suggests the binding of isolated atoms, for which adsorbate density is expected to increase linearly with metal exposure while maintaining a homogeneous size-distribution.

While the previous figures show a clear preference for Au binding exclusively within amorphous areas of the film, domain boundaries present an exception to the general rule. As can be seen by STM (Figure 4b), Au features decorate the boundary

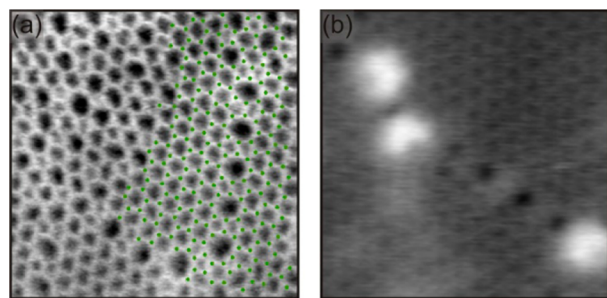


Figure 4. (a) nc-AFM image showing amorphous and crystalline domains (7 × 7 nm², V_S = 50 mV, constant height). Green symbols mark the Si positions around the domain boundary. Domain boundaries consist of 8-membered rings alternating with pairs of 5-membered rings. (b) STM image of a domain boundary after Au adsorption (7 × 7 nm², V_S = 2 V, I_T = 100 pA).

separating two domains within an entirely crystalline area of the film. In addition to the smaller structures shown here, larger Au features were also found at these sites, which we ascribe to the formation of small clusters. This type of behavior is consistent with Au adsorption studies conducted over Mo(112) supported monolayer silica films, where Au adsorption was only detected at the domain boundaries within the otherwise defect-free films.⁸ For reference, a higher resolution nc-AFM image of such a domain boundary is provided in Figure 4a, which clearly shows the presence of alternating 5- and 8-membered rings at the boundary between two crystalline domains.

Given the similarities between the termination of our film and the monolayer version investigated previously, it would be

reasonable to expect Au and Pd atoms to diffuse into the pores of the honeycomb network, as was the case in the former studies.⁸ Such a process would be consistent with the observed Au and Pd stability and might provide suitable explanations for the phase-indifferent and phase-specific binding of Pd and Au, respectively. (Over crystalline areas, we expect large barriers to inhibit the diffusion of Au into the 6-membered rings, whereas film penetration within domain boundaries and amorphous areas might occur, so long as sufficiently large pores are available within those structures. By contrast, Pd would be expected to readily enter 6-membered rings, which make up the majority of both phases, and as such, we would expect an equal probability for binding over the entire surface.)

Provided binding is facilitated by pore entry, we must now consider a set of options that were not possible over the monolayer film, where subsurface diffusion implied adhesion to the underlying metal substrate. By changing from a monolayer to a decoupled bilayer structure, we create the possibility for metal adsorption within the bilayer cages created by the vertical Si–O–Si bonds linking the upper and lower hexagonal termini. This and the validity of our pore-entry-mediated adsorption hypothesis will be discussed further in the following sections.

3.2. Photoemission Studies. **3.2.1. Support Effects.** To better understand the nature of the metal–support interactions between the bilayer film and Pd or Au adsorbates, we have probed the electronic structure of such samples using XPS. Figure 5 shows results from measurements of the work-functions, O 1s and Si 2p core-levels, and Si K₁L₂₃L₂₃ Auger spectra for SiO₂/Ru samples following preparation (gray), after conversion to “O-poor” upon heating to ~1175 K in UHV (black),²⁵ and with small amounts of Au (red, ~2.2 × 10¹³ atoms/cm⁻² ≈ 0.02 monolayer equivalents [MLE]) or Pd (blue, ~6.8 × 10¹³ atoms/cm⁻² ≈ 0.05 MLE) adsorbed at ~150 K. By visual inspection, it is readily apparent that both Au and Pd adsorption result in spectroscopic changes that are qualitatively similar to those noted after reversibly removing some ruthenium-bound oxygen from freshly prepared SiO₂/Ru samples. In the case of metal adsorption, however, the SiO₂ related peak-shifts are not accompanied by attenuations of the O–Ru shoulder, located at ~530 eV in the O 1s spectra, which implies that these shifts really result from interaction with the metal species rather than coincidental loss of oxygen.

To more readily track the changes in Figure 5, we note the shifts for the work-function Φ, O 1s (main peak), Si 2p, and Si K₁L₂₃L₂₃ features after adding 0.02 MLE Au, 0.05 MLE Pd, and 0.24 MLE Pd, and creating the O-poor film in Table 1. In every case, we note shifts to lower kinetic energy (KE) after altering the sample. While the size of the shifts varies from case to case, the features always appear to move as a unit, such that every peak shifts by roughly the same ΔKE after employing a given condition. For Pd, the size of these shifts scales with loading, which implies that the effect causing the changes does not saturate within this coverage regime.

By comparing the change in the KE of the Si K₁L₂₃L₂₃ peaks with the corresponding Si 2p binding energy (BE) shifts, we can use an Auger parameter analysis (see below) to determine energy contributions for the final-state relaxation, which turn out to be negligible in every case. If we assume the same degree of final-state contribution to the O 1s shifts, then we can create orbital-energy diagrams depicting the changes to the electronic structure of the SiO₂/Ru system corresponding to each modification. Such an illustration is provided in Figure 6, which shows the Fermi-referenced energies of the vacuum level

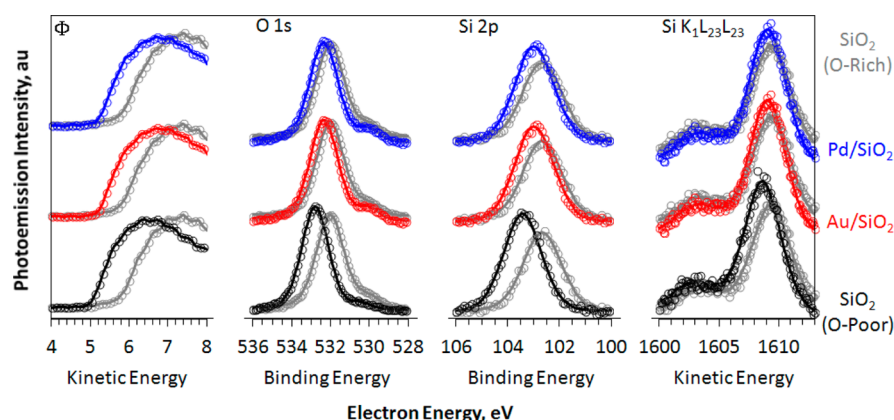


Figure 5. XP spectra collected over energy regions corresponding to the threshold for the escape of inelastically scattered electrons (Φ), O 1s and Si 2p core-level photoemission, and Si $K_1L_{23}L_{23}$ Auger transitions are provided for freshly prepared SiO_2/Ru (gray), oxygen deficient SiO_2/Ru (black), 0.02 MLE Au (red), and 0.05 MLE Pd (blue). Metal adsorption was conducted at $T \approx 150$ K.

Table 1. Shifts in the KEs of the Threshold for the Escape of Inelastically Scattered Electrons (Φ), O 1s and Si 2p BEs, Si $K_1L_{23}L_{23}$ KEs, and Final-State Relaxation Contributions (ΔR_f) at ~ 150 K, Reported in eV

| | $\Delta\Phi$ | $\Delta\text{O } 1s$ | $\Delta\text{Si } 2p$ | $\Delta\text{Si } K_1L_{23}L_{23}$ | ΔR_f |
|-----------------------------|--------------|----------------------|-----------------------|------------------------------------|--------------|
| O-Poor SiO_2 | -0.8 | +0.77 | +0.77 | -0.74 | ~ 0 |
| 0.02 MLE Au/ SiO_2 | -0.5 | +0.32 | +0.32 | -0.31 | ~ 0 |
| 0.05 MLE Pd/ SiO_2 | -0.5 | +0.32 | +0.31 | -0.30 | ~ 0 |
| 0.24 MLE Pd/ SiO_2 | -1.2 | +1.40 | +1.45 | N/A* | N/A* |

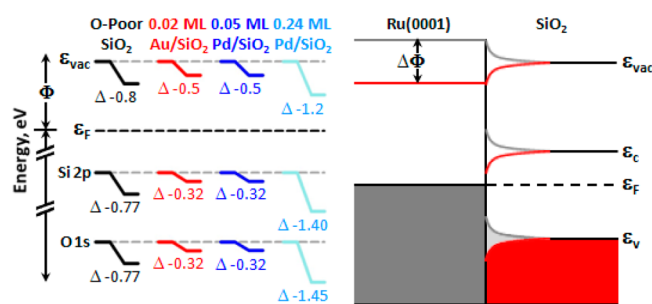


Figure 6. (left) Orbital-energy diagrams depicting the relative positions of the vacuum level, Fermi level, Si 2p orbital, and O 1s orbital are shown for each of the conditions examined in Table 1. For reference, these positions are plotted relative to their energies in the pristine SiO_2/Ru sample (gray lines). (right) A qualitative depiction of band-bending at the SiO_2 -Ru interface is shown as a function of work-function (gray vs red). For clarity, the horizontal dimension denotes distance traveled perpendicular to the interface, and the vertical dimension reflects energy.

and Si 2p and O 1s orbitals for freshly prepared (gray), O-poor (black), 0.02 MLE Au (red), 0.05 MLE Pd (blue), and 0.24 MLE Pd (light blue) SiO_2/Ru samples.

From this, it is relatively straightforward to conclude that variations in the degree of band-bending almost entirely account for the changes in SiO_2 electronic structure following the investigated modifications.³² For clarity, a qualitative depiction of this effect is included next to the orbital-energy diagram in Figure 6. As can be seen, any changes to the system that result in a decreased (increased) work-function will always decrease (increase) the energy of the band structure within the oxide near the metal-oxide junction, which means the entire film in our case, as the oxide is only bilayer thick. This interpretation is consistent with previous models of the O-rich versus O-poor systems,²⁵ and the work-function changes

suggest that both Au and Pd bind in a manner that results in charge-transfer from the metals to the Ru support. In fact, according to the classical picture proposed by both Kingdom and Langmuir (1923) and Gurney (1935), Φ decreases for positively charged adsorbates on metal surfaces because image charges form within the metals, which give rise to dipole layers that emitted electrons must then pass through.^{33,34}

3.2.2. Pd and Au Effects. To further explore the nature of the binding processes discussed above, we have also investigated the electronic structure of the adsorbed metals. Results from this work are provided in Figure 7, which shows

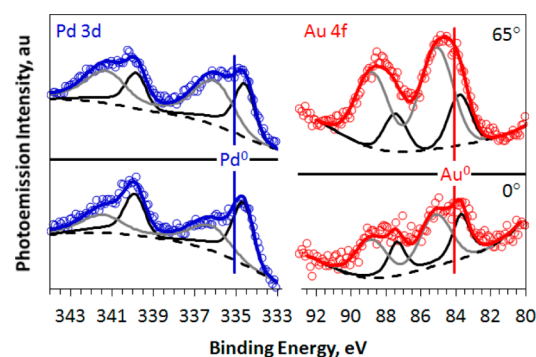


Figure 7. XPS spectra for 0.05 MLE Pd (left) and 0.02 MLE Au (right) are shown for different collection angles (relative to the surface normal). Both samples are identical to those used to create Figure 5, and background shapes (dashed lines) result from a combination of uncovered SiO_2/Ru and Shirley background contributions. For clarity, small features assigned to Pd plasmon resonances have been omitted from this figure. Such features show up at ~ 341 eV and contribute to $<10\%$ of the total Pd 3d fit (see below).

core-level XPS spectra from the Pd 3d and Au 4f orbitals of the respective metals after adsorption under the same conditions used to generate Figure 5. Starting with the lower spectra, which show XPS results collected along the surface normal, we clearly note the presence of two distinct features in each case, with one at higher- and the other at lower-than-bulk BE. While the features at higher BEs may result from any combination of several effects (i.e., reduced final-state screening,³⁵ lattice contraction,³⁶ charge-transfer to the surface, and/or adventitious adsorption of background gases like H_2 ,³⁷ H_2O ,³⁸ or CO),³⁹ there are relatively few effects that would be expected to

shift the BEs of supported metals to values *lower* than those from bulk samples. Classical XPS interpretation, based on (initial-state) charge screening effects, would suggest an accumulation of negative charge on these Pd and Au species, which could potentially contradict our explanations of the work-function shifts discussed above. Alternatively, hybridization effects, like those responsible for surface core-level-shifts, might play a role here, and will be further discussed in the theory section below.⁴⁰ Notably, the positions of both peaks (Pd at ~ 334.7 eV, and Au at ~ 83.6 eV) are consistent with values reported for surface core-level-shifts from Pd and Au samples, respectively.^{40,41}

When shifting to more grazing collection angles (top spectra), we note relative growth of the higher BE components, indicating that these features relate to atoms bound at the surface. By contrast, the relative intensity of the lower BE components decline at the more grazing collection angle, suggesting that these features correspond to metal atoms that have diffused into the pores of the silica-network to find stable binding sites below the surface of the film.⁴¹ Since our STM results suggest that surface SiO₂ adsorption sites are not the most favorable, we can assume that binding in this manner most likely occurs at special metal nucleation sites, such as film defects or small clusters formed by happenstance prior to stable atomic binding within the pores. This assumption could help explain the increased relative intensity of the higher BE component for the Au samples relative to their *more concentrated* Pd covered counterparts. If we trust the conclusions of our STM studies (that gold cannot enter the 6-membered rings, which make up the majority of our samples), then it would follow that Au atoms (especially those initially binding over crystalline domains) would necessarily need to explore larger areas of the silica surface before locating stable subsurface binding sites and, as such, would be more likely to first encounter other adatoms to form surface-bound clusters instead. Unfortunately, technical limitations related to the metal fluxes attainable from our microevaporators and surface cleanliness after warming the sample prevented us from directly observing such effects under similar conditions within the STM studies.

To further investigate our tentative peak assignments, we provide Figure 8, which shows the Pd 3d XPS dependence on loading. From this, we note a few effects upon increasing the Pd coverage from 0.06 to 0.24 MLE. First, both the position and width of the lower BE feature remain roughly unchanged, which implies that Pd species entering the film remain reasonably isolated under these conditions. Second, the position of the higher BE component shifts to lower values and grows relative to the other peak with increasing coverage. These effects can be rationalized following our competitive binding mechanism proposed earlier. Since both samples were created in roughly the same amount of time, higher loading also means higher flux, and because of this, the likelihood for happenstance cluster formation is expected to be greater for the higher coverage sample. Furthermore, the presence of more Pd means that these clusters will likely be larger in size than their counterparts on the low-coverage sample. Combining these effects, we should expect greater relative intensities and lower BEs for this peak, with increasing final-state relaxation and lattice expansion contributions, as the SiO₂ surface-bound clusters grow in both average size and relative abundance.³⁶ To the degree that the electrostatic interactions governing band-bending within the SiO₂ should also influence the electronic

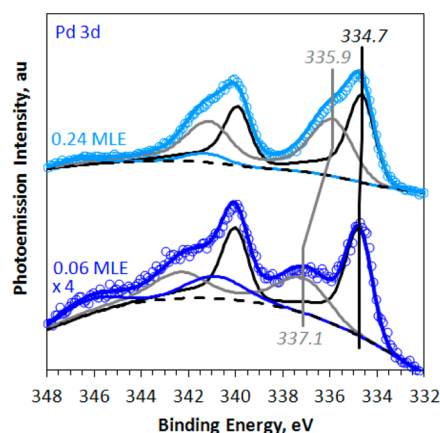


Figure 8. XPS spectra are shown for Pd/SiO₂/3O-(2 × 2)/Ru(0001) samples created via exposure to 0.06 and 0.24 MLE Pd at ~ 150 K. We include fits of the plasmon component (blue), which is needed to account for features near 346 eV and has been fit using the same spin-orbit splitting and ratio as the other Pd 3d features.

structure of the supported metals, albeit to a lesser extent, we might expect counteracting relative contributions to the initial-state BEs of the silica-bound Pd with increasing coverage, which would imply that the other effects contribute to coverage-dependent Δ BEs somewhat larger than the observed shift in XPS peak position. Perhaps not unexpectedly, similar effects were also noted when increasing the sample temperature during doses with equivalent fluxes and coverages, as this effectively increases the area that each atom explores prior to subsurface adsorption.

To better interpret our core-level findings and compare our results with those from theoretical studies (see below), we have conducted Auger parameter analysis of both systems using core–core–core transitions with final-states containing two holes in the same orbitals probed by XPS (Figure 9). For Au 4f

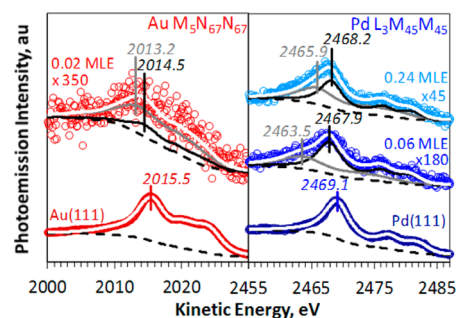


Figure 9. Au M₅N₆₇N₆₇ and Pd L₃M₄₅M₄₅ spectra are provided for various Au and Pd covered samples ($T_{\text{ads}} \approx 150$ K). The Pd samples correspond to those used in Figure 8, while XPS data for the Au sample is not provided (similar to that shown in Figure 7). The curves provided in the fits of the Pd/SiO₂ and Au/SiO₂ samples correlate to the high (gray) and low (black) BE components of the corresponding XPS fits from the same samples. For comparison, Au(111) and Pd(111) data are also included at the bottom of the figure.

and Pd 3d, these are the Au M₅N₆₇N₆₇ and Pd L₃M₄₅M₄₅ lines, which show peaks at ~ 2015.5 and ~ 2469.1 eV for the bulk metals (lower spectra). Using the peak shapes from the pure metals, we have fit the remainder of the spectra by varying the positions and widths of two peaks, whose relative intensities are equal to those from the features in corresponding XPS spectra.

On the basis of the positions of those peaks, in conjunction with the shifts in the corresponding XPS spectra, we can calculate the final-state relaxation contributions to the previously discussed BE shifts using the following equation, which has been derived using methods described elsewhere:^{42,43}

$$\Delta R_i = 1/2(\Delta\alpha) = 1/2(\Delta BE_i + \Delta KE_{jii}) \quad (1)$$

Here, R_i is the relaxation contribution to the final-state of a photoemission process involving emission from the i th orbital, and α is the Auger parameter, which is equal to the BE from the i th orbital's photoemission peak added to the KE of the corresponding Auger peak. For a detailed experimental and theoretical treatment of the Auger parameter and its application to this particular system, please see ref 44.

Using this approach, we have created Table 2, which partitions the relative shifts of the two XPS components into

Table 2. Shifts in the Pd 3d and Au 4f Core-Level BEs, Auger KEs, Orbital Relaxation Energies (ΔR_i), and Initial-State Orbital Energies for Atoms Binding in a Fashion Giving Rise to the High (Gray) and Low (Black) BE Features Noted in the XPS Spectra; All Values Are Relative to Those from Metal Single-Crystals and Are Listed in eV

| | ΔBE | ΔKE | ΔR_i | $\Delta \varepsilon_i^a$ |
|------------------------------|-------------|-------------|--------------|--------------------------|
| 0.02 MLE Au/SiO ₂ | +1.00 -0.36 | -2.26 -0.96 | -0.63 -0.66 | -0.37 +1.02 |
| 0.06 MLE Pd/SiO ₂ | +2.08 -0.30 | -5.64 -1.24 | -1.78 -0.77 | -0.30 +1.07 |
| 0.24 MLE Pd/SiO ₂ | +0.84 -0.40 | -3.24 -0.94 | -1.20 -0.67 | +0.36 +1.07 |

$$^a \Delta \varepsilon_i = -(\Delta BE + \Delta R_i).$$

their respective initial- ($\Delta \varepsilon_i$) and final-state (ΔR_i) orbital-energy contributions for the various Au and Pd covered samples explored in Figure 9. Clearly, low signal-to-noise ratios result in a fair amount of flexibility for the absolute positioning of the individual components, such that we estimate approximate uncertainties of ± 0.5 and 0.1 eV for the individual Auger and XPS fits, respectively (i.e., $\sim \pm 0.3$ eV for ΔR_i and $\Delta \varepsilon_i$). This, however, is unavoidable, given the need to make use of small coverages and Bremsstrahlung radiation, which are necessary because larger coverages increasingly favor clustering, and the energy required to excite the appropriate Auger transitions exceeds that of our nominal Al K α line.

Nonetheless, some interesting trends are abundantly clear upon inspection of the tabulated data. Starting with the lower BE components (black), which have been assigned to metal species penetrating the pores of the film, we note roughly the same behavior in all cases. Whether from gold or palladium, at higher or lower coverages, this feature is always sharp (FWHMs comparable with those from single-crystals) and shifted by ~ 0.35 eV relative to reference Au 4f and Pd 3d XP spectra. Combining this with the similar Auger shifts, we calculate nearly identical final- and initial-state contributions to the ΔBE s in each case, such that the core-levels of either element shift upward (toward ε_F) by ~ 1 eV when binding in this manner.

By contrast, the higher BE component (gray), assigned to metal binding over the SiO₂ support, shows reasonable variation as a function of adsorbate and coverage. In general, those samples exhibiting greater relative intensities of this feature also show smaller decreases in the degree of final-state relaxation, and this reflects a greater propensity for the formation of larger clusters, which more effectively screen the core-hole created by the photoemission process.³⁵ After

correcting for these effects, we note nearly neutral metal species in all cases, albeit with a significant orbital-energy increase of ~ 0.6 eV when increasing the Pd coverage by a factor of 4. Qualitatively, this increase is consistent with supported cluster growth, where larger structures are expected to show less negative (closer to ε_F) orbital energies due to lattice expansion effects.²³

3.3. Density Functional Theory Calculations. **3.3.1. Pd and Au Adsorption on SiO₂ Films.** The interfacial distance calculated between the crystalline SiO₂ bilayer and the oxygen covered 3O-(2 \times 2)/Ru(0001) surface is 3.76 Å (computed from the bottom oxygen layer of SiO₂ to the Ru surface layer), which is indicative of a weak interaction and compares well with previous DFT-D2 results for this system.²⁵ The work-function of our SiO₂/3O-(2 \times 2)/Ru(0001) model system is 6.26 eV, which is about 1.3 eV higher than that of the bare Ru(0001) surface (4.94 eV). We again note that the latter value is underestimated with respect to experimentally derived values (5.4 eV),²⁹ as pointed out in section 2.2. The increased Φ of the SiO₂ model system (relative to bare Ru) is essentially related to the adsorption of oxygen at the interface ($\Phi_{3O-(2 \times 2)/Ru(0001)} = 6.25$ eV), as the presence of the decoupled stoichiometric oxide film exhibits only minor effects on the work-function.

An adsorbed Pd atom interacts weakly with the surface of the crystalline silica film, with the adsorption energy being dominated by VdW contributions, which are at their largest when Pd is located in the center of one of the silica rings ($E_{\text{ads}} = -1.13$ eV; where $E_{\text{ads}} = E_{\text{M/film}} - E_{\text{M}} - E_{\text{film}}$, such that a negative value indicates an exothermic adsorption). By contrast, a sizable energy gain is obtained when the Pd atom is adsorbed at the SiO₂/Ru interface. Here, Pd binds preferentially to the Ru 3-fold hollow site not occupied by oxygen atoms, as shown in Figure 10, with $E_{\text{ads}} = -3.60$ eV. This stable configuration

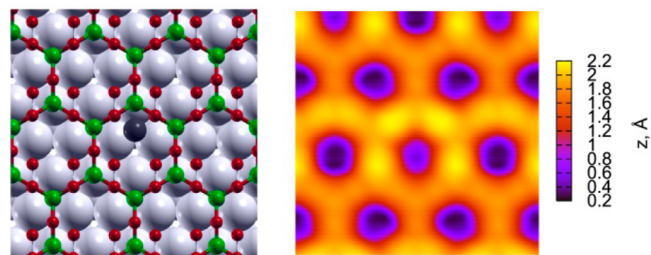


Figure 10. Pd atom adsorbed at the interface between SiO₂ and the 3O-(2 \times 2)/Ru(0001) surface. (a) Ball and stick representation (green, red, light gray, and dark gray represent Si, O, Ru, and Pd atoms, respectively). (b) Simulated STM image (1.64 nm \times 1.64 nm; $V = 1.5$ V; isodensity = 5×10^{-7} e/Å³; $z = 0$ at the top oxygen layer of SiO₂ film).

can be reached with a negligible energy barrier (< 0.1 eV). We note that the off-center adsorption site, with respect to the silica ring, is compatible to the “butterfly” experimental STM images, showing that the Pd related features, which we ascribe to a change in the SiO₂ density of states (DOS) induced by interfacial adatoms, are not symmetric along the ring (Figure 10).

The adsorption of an Au atom on the crystalline silica surface also gives rise to a weak adsorption, $E_{\text{ads}} = -0.52$ eV, with the preferred adsorption site in the center of the ring where the dispersion interaction is maximized. Au also binds strongly at the metal/metal–oxide interface, $E_{\text{ads}} = -2.58$ eV, although the

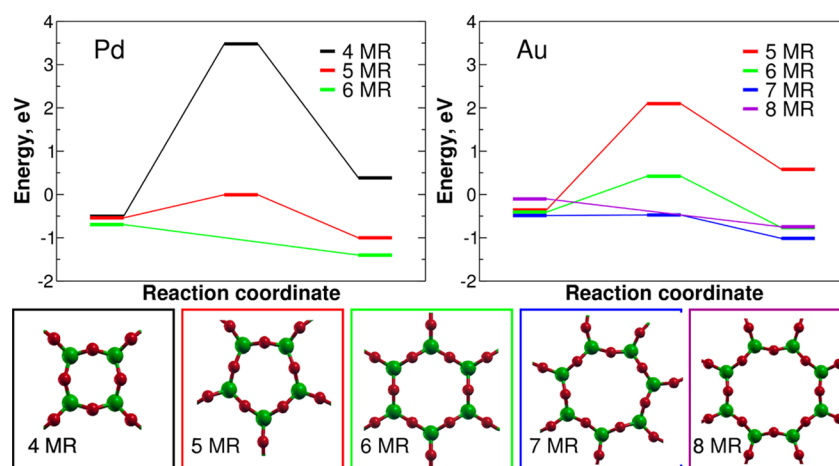


Figure 11. Penetration profiles for Pd and Au through rings of different size. Energies are computed with respect to the metal atom in the gas phase. In the bottom panels the n MR SiO₂ rings are reported ($n = 4-8$; green and red represent Si and O atoms, respectively).

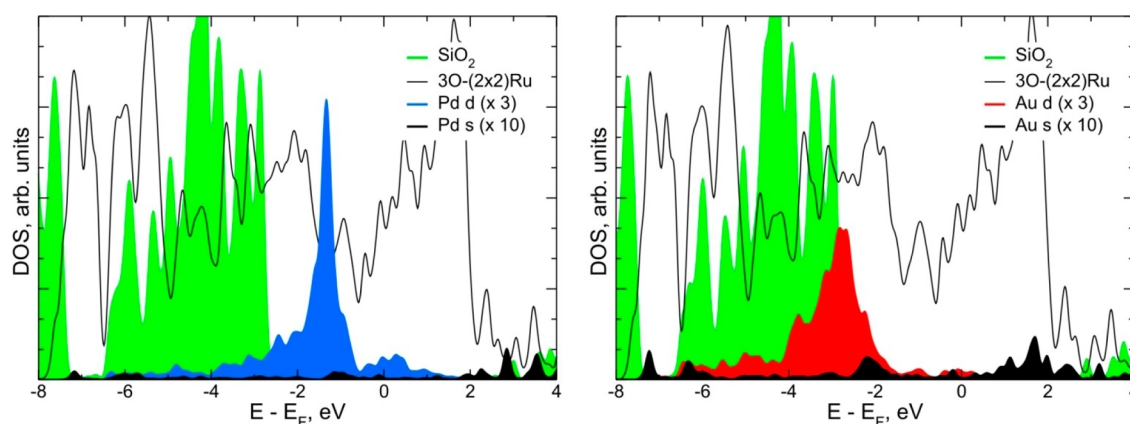


Figure 12. Density of states (DOS) for Pd (left) and Au (right) atoms adsorbed at the interface between SiO₂ and the 3O-(2 × 2)/Ru(0001) surface. Projected DOS on s and d Pd and Au states, on the SiO₂ film, and of the interfacial O and the first Ru layer (solid grey line) are displayed.

interaction is weaker than in the Pd case. The main difference between Pd and Au is that Au penetration into the silica pores is an activated process with a relatively high energy barrier (0.82 eV for an unsupported SiO₂ bilayer). For the Ru supported film a barrier of 0.5 eV has been computed for penetration into the first silica layer, while a smaller barrier (0.2 eV) remains for subsequent diffusion of Au from inside the SiO₂ cage to the interface.

3.3.2. Pd and Au Barriers for Interfacial Adsorption as a Function of Ring Size. Unlike the crystalline phase, which is formed exclusively by 6-membered rings (6MR), the amorphous patches of the film contain rings of different sizes, ranging from 4MR up to 9MR.¹² To explore the energy profiles and barriers for Pd and Au diffusion into the amorphous phase, we have performed a series of calculations using the unsupported cluster models provided in Figure 11. We have verified that these models provide the same energy barriers obtained for unsupported silica films, with errors within 0.02 eV. Compared to supported films, we have to point out that because some depopulation of the 6s state occurs for Au adsorbed on the SiO₂/3O-(2 × 2)/Ru(0001) surface, which facilitates atom penetration, the barrier of the unsupported models are somewhat overestimated (for 6MR the surface penetration barriers are 0.8 eV for unsupported and 0.5 eV for supported films, respectively).

Pd atoms can reach the cage center via a nonactivated process for n MR with $n \geq 6$, while a barrier of 0.53 eV is required for the 5MR. The Pd binding energy inside the cage, -1.40 eV for 6MR, decreases with the reduction of the cage size due to steric repulsion effects. For 4MR the barrier is very high (>3 eV) and E_{ads} inside the cage is positive, $+0.38$ eV, indicating that no diffusion can occur through these small rings.

In the case of Au, penetration through the 5MR is already unfavorable (barrier > 2.5 eV and $E_{\text{ads}} = +0.58$ eV). The interaction outside and inside the ring becomes slightly more favorable by increasing the ring size into the 5–7 MR range, as the barrier drops considerably and becomes <0.1 eV for the 7MR (Figure 11). For the 8MR there is no longer any penetration barrier, and the interaction with the oxide becomes negligible on the surface (-0.10 eV) and small, but non-negligible, inside the cage (-0.75 eV). This effect is expected to be even more pronounced for n MR with $n \geq 9$, where both Pd and Au atoms penetrate without barriers. Inside large cages, the adsorbate assumes a central position with larger distances from the O atoms to reduce steric repulsion. In this way, the VdW forces are reduced and only weak interactions are expected.

While the binding energy inside of the silica bilayer cages never exceeds -1.5 eV, a much stronger interaction is found at the oxide–metal interface. This suggests that metal atoms can hardly be stabilized inside the pores since the atoms that penetrate through the oxide surface with small barriers will

easily reach the interface. These results are consistent with the experimental findings, which indicate a propensity for Pd penetration through both phases of the SiO₂ films and Au incorporation only at grain boundaries or amorphous areas, where larger rings can be found.

3.3.3. Electronic Properties of Pd and Au Atoms at the SiO₂/3O-(2 × 2)/Ru(0001) Interface. The optimal binding location of a Pd atom at the SiO₂/Ru interface is at an unoccupied 3-fold hollow site (Figure 10), and the projected DOS for this configuration is reported in Figure 12, which shows that the Pd 5s state is empty, while the 4d states are not completely filled due to strong hybridization with Ru states. The Bader charge on Pd, +0.32|e|, indicates a partial charge transfer from Pd to the substrate, and no magnetic moment is found on Pd. Pd incorporation at the interface induces a decrease of the work-function by −0.96 eV, consistent with electron transfer from Pd to Ru. While the direction of this change reproduces the experimental observations, the magnitude of the effect depends on the Pd coverage considered, and as such, the computed shift cannot be directly compared with the experimental results but is also qualitatively consistent with the coverage-dependent trends noted in section 3.2.1.

The Pd 3d CLS computed in the initial-state approximation indicates a shift toward smaller binding energies (−0.67 eV), with respect to bulk Pd. The inclusion of final-state effects reduces the shift to −0.42 eV. This is in good agreement with the experimentally observed shifts. In particular, a total shift of −0.30 eV is found by XPS for the low energy peak at 0.06 ML coverage and has been attributed to isolated Pd atoms at the interface (Table 2). Consistent with the Auger decomposition, our computational results also indicate that this observable shift largely originates from initial-state (rather than final-state) contributions.

Because of the high work-function of the substrate, the electronegative Au atom also partly oxidizes when adsorbed at the interface, and the projected DOS clearly indicates a partial emptying of the 6s state, compared to the 6s¹ occupation of the neutral atom. Hybridization with the Ru states causes a quenching of the Au magnetic moment, and the Bader charge (+0.24|e|) is similar to that of Pd, causing a comparable work-function change (−1.07 eV). The latter effects again confirm partial charge-transfer from the adatom toward the substrate. Additionally, the effect on the core-level is similar to the Pd case, with the initial-state Au 4f CLS being −0.84 eV, which is again reasonably consistent with the experimental results relating to those atoms assigned to subsurface binding configurations.

As mentioned previously, our negative (initial-state governed) CLSs are typically interpreted to be an indication of increased electron density around the Pd or Au atoms, but this would be in direct contrast with the computed Bader charges and work-function changes. Indeed, our negative CLSs have a completely different origin, which has been discussed within the literature pertaining to surface versus bulk CLSs in metals and thoroughly detailed for the Pd/SiO₂/Ru system elsewhere.^{44,45} Put simply, the atomically dispersed metal adatoms (whether Au or Pd), which are present at the SiO₂/Ru interface of our samples, adopt less d–sp hybridized electronic configurations, relative to their reference sample counterparts, due to their decreased coordination, which is consistent with the emptying of the 5s and 6s states depicted in the projected DOSs for Pd and Au in Figure 12. As more electron density is transferred from higher lying, more diffuse s-orbitals into lower lying, more

contracted d-levels, the electrostatic potential at the nucleus of our less-coordinated atoms changes in a manner that results in the observed upward orbital-energy shifts (relative to the more-coordinated atoms in the bulk reference samples). At the same time, decreasing the metal–metal coordination of these atoms also results in less extra-atomic screening due to the decreased density of conduction-band electrons. The fact that the observed BE shifts for our samples remain negative simply indicates that the former effect outweighs the decreases in extra-atomic screening and local charge density (from charge-transfer) at the metal sites.

4. CONCLUSIONS

Using a combination of STM, nc-AFM, XPS, and theory, we have investigated the preferred binding mechanisms for Au and Pd over bilayer SiO₂/Ru(0001) supports at low temperatures. It appears that both metals prefer binding at the Ru interface after diffusing through the film, but do so with differing probabilities due to differing pore-size-dependent entry barriers. While Pd may freely diffuse through pores within both crystalline and amorphous domains of the film, Au cannot enter the 6-membered rings that comprise the ordered phase but instead binds exclusively within amorphous areas and domain boundaries, which possess larger ring structures. In this way, the film acts as a flexible atomic sieve, which may be tuned by controlling its crystallinity.

With increasing temperature and coverage, we note an increased likelihood for forming silica-bound clusters, which is presumably due to the enhanced probability of multiple atom collisions during the diffusion period prior to pore-entry and stable binding. While the surface-bound clusters appear to be effectively neutral, the atoms penetrating the film exhibit strong core-level-shifts to smaller binding energies. These shifts result predominantly as a consequence of the lower coordination, and resultant rehybridization, of the Au and Pd atoms compared to their bulk counterparts, rather than charge-transfer effects, and both metals appear to actually donate (rather than withdraw) charge to (from) the Ru surface. Consistent with this observation, introduction of either metal acts to reduce the work-function of the sample, which, in turn, alters the degree of band-bending at the SiO₂–Ru interface in a manner similar to that noted previously upon the removal of small amounts of ruthenium-bound oxygen.²⁵

AUTHOR INFORMATION

Corresponding Authors

* (M.H.) E-mail: heyde@fhi-berlin.mpg.de.

* (W.E.K.) E-mail: kaden@fhi-berlin.mpg.de.

Present Addresses

[§] (L.L.) Lawrence Berkeley National Laboratory, 1 Cyclotron Road, Berkeley, California 94720, United States.

^{||} (F.R.) Leibniz-Institut für Kristallzüchtung, Max-Born-Strasse 2, 12489 Berlin, Germany.

Notes

The authors declare no competing financial interest.

ACKNOWLEDGMENTS

W.E.K. thanks the Alexander von Humboldt Foundation for their financial support of this work. F.R. and M.S. would like to acknowledge support from the European Research Council for project number 280070 within the FP7-IDEAS-ERC program. L.G. and G.P. thank Italian MIUR for support through the

FIRB Project RBAP115AYN "Oxides at the nanoscale: multifunctionality and applications". The COST Action CM1104 "Reducible oxide chemistry, structure and functions" is also gratefully acknowledged.

REFERENCES

- (1) Giordano, L.; Pacchioni, G. Oxide Films at the Nanoscale: New Structures, New Functions, and New Materials. *Acc. Chem. Res.* **2011**, *44*, 1244–1252.
- (2) Xu, Y.; Ma, J.; Xu, Y.; Xu, L.; Li, H.; Li, H. Palladium Nanoparticles Encapsulated in Porous Silica Shells: An Efficient and Highly Stable Catalyst for CO Oxidation. *RSC Adv.* **2013**, *3*, 851–858.
- (3) Celik, F. E.; Kim, T.-J.; Bell, A. T. Effect of Zeolite Framework Type and Si/Al Ratio on Dimethoxymethane Carbonylation. *J. Catal.* **2010**, *270*, 185–195.
- (4) Shaikhutdinov, S.; Freund, H.-J. Ultrathin Silica Films on Metals: The Long and Winding Road to Understanding the Atomic Structure. *Adv. Mater.* **2013**, *25*, 49–67.
- (5) Weissenrieder, J.; Kaya, S.; Lu, J.-L.; Gao, H.-J.; Shaikhutdinov, S.; Freund, H.-J.; Sierka, M.; Todorova, T.; Sauer, J. Atomic Structure of a Thin Silica Film on a Mo(112) Substrate: A Two-Dimensional Network of SiO₄ Tetrahedra. *Phys. Rev. Lett.* **2005**, *95*, 076103.
- (6) Giordano, L.; Ricci, D.; Pacchioni, G.; Ugliengo, P. Structure and Vibrational Spectra of Crystalline SiO₂ Ultra-Thin Films on Mo(112). *Surf. Sci.* **2005**, *584*, 225–236.
- (7) Ulrich, S.; Nilius, N.; Freund, H.-J.; Martinez, U.; Giordano, L.; Pacchioni, G. Evidence for a Size-Selective Adsorption Mechanism on Oxide Surfaces: Pd and Au Atoms on SiO₂/Mo(112). *ChemPhysChem* **2008**, *9*, 1367–70.
- (8) Ulrich, S.; Nilius, N.; Freund, H.-J.; Martinez, U.; Giordano, L.; Pacchioni, G. Realization of an Atomic Sieve: Silica on Mo(112). *Surf. Sci.* **2009**, *603*, 1145–1149.
- (9) Boscoboinik, J. A.; Yu, X.; Yang, B.; Shaikhutdinov, S.; Freund, H.-J. Building Blocks of Zeolites on an Aluminosilicate Ultra-Thin Film. *Microporous Mesoporous Mater.* **2013**, *165*, 158–162.
- (10) Yu, X.; Yang, B.; Boscoboinik, J. A.; Shaikhutdinov, S.; Freund, H.-J. Support Effects on the Atomic Structure of Ultrathin Silica Films on Metals. *Appl. Phys. Lett.* **2012**, *100*, 151608.
- (11) Löffler, D.; Uhlrich, J. J.; Baron, M.; Yang, B.; Yu, X.; Lichtenstein, L.; Heinke, L.; Büchner, C.; Heyde, M.; Shaikhutdinov, S.; et al. Growth and Structure of Crystalline Silica Sheet on Ru(0001). *Phys. Rev. Lett.* **2010**, *105*, 146104.
- (12) Lichtenstein, L.; Büchner, C.; Yang, B.; Shaikhutdinov, S.; Heyde, M.; Sierka, M.; Włodarczyk, R.; Sauer, J.; Freund, H.-J. The Atomic Structure of a Metal-Supported Vitreous Thin Silica Film. *Angew. Chem., Int. Ed.* **2012**, *51*, 404–407.
- (13) Yang, B.; Kaden, W. E.; Yu, X.; Boscoboinik, J. A.; Martynova, Y.; Lichtenstein, L.; Heyde, M.; Sterrer, M.; Włodarczyk, R.; Sierka, M.; et al. Thin Silica Films on Ru(0001): Monolayer, Bilayer and Three-Dimensional Networks of [SiO₄] Tetrahedra. *Phys. Chem. Chem. Phys.* **2012**, *14*, 11344–11351.
- (14) Zachariasen, W. H. The Atomic Arrangement in Glass. *J. Am. Chem. Soc.* **1932**, *54*, 3841–3851.
- (15) Grimley, D. L.; Wright, A. C.; Sinclair, R. N. Neutron Scattering from Vitreous Silica IV. Time-of-Flight Diffraction. *J. Non-Cryst. Solids* **1990**, *119*, 49–64.
- (16) Mozzi, R. L.; Warren, B. E. The Structure of Vitreous Silica. *J. Appl. Crystallogr.* **1969**, *2*, 164–172.
- (17) Rust, H.-P.; König, T.; Simon, G. H.; Nowicki, M.; Simic-Milosevic, V.; Thielsch, G.; Heyde, M.; Freund, H.-J. A Portable Microevaporator for Low Temperature Single Atom Studies by Scanning Tunneling and Dynamic Force Microscopy. *Rev. Sci. Instrum.* **2009**, *80*, 113705.
- (18) Powell, C. J.; Jablonski, A. *NIST Electron Effective-Attenuation-Length Database*; National Institute of Standards and References: Gaithersburg, MD, 2011.
- (19) Kresse, G.; Furthmüller, J. Efficient Iterative Schemes for Ab Initio Total-Energy Calculations Using a Plane-Wave Basis Set. *Phys. Rev. B* **1996**, *54*, 11169–11186.
- (20) Kresse, G.; Hafner, J. Ab Initio Molecular Dynamics for Liquid Metals. *Phys. Rev. B* **1993**, *47*, 558–561.
- (21) Blöchl, P. E. Projector Augmented-Wave Method. *Phys. Rev. B* **1994**, *50*, 17953–17979.
- (22) Perdew, J. P.; Burke, K.; Ernzerhof, M. Generalized Gradient Approximation Made Simple. *Phys. Rev. Lett.* **1996**, *77*, 3865–3868.
- (23) Grimme, S. Semiempirical GGA-Type Density Functional Constructed with a Long-Range Dispersion Correction. *J. Comput. Chem.* **2006**, *27*, 1787–1799.
- (24) Amft, M.; Lebègue, S.; Eriksson, O.; Skorodumova, N. V. Adsorption of Cu, Ag, and Au Atoms on Graphene Including van der Waals Interactions. *J. Phys.: Condens. Matter* **2011**, *23*, 395001.
- (25) Włodarczyk, R.; Sierka, M.; Sauer, J.; Löffler, D.; Uhlrich, J. J.; Yu, X.; Yang, B.; Groot, I. M. N.; Shaikhutdinov, S.; Freund, H.-J. Tuning the Electronic Structure of Ultrathin Crystalline Silica Films on Ru(0001). *Phys. Rev. B Condens. Matter Mater. Phys.* **2012**, *85*, 085403.
- (26) Morozkin, A. V.; Seropegin, Y. D. Sm–Ru–Ge System at 1070 K. *J. Alloys Compd.* **2004**, *365*, 168–172.
- (27) Henkelman, G.; Jónsson, H. A Dimer Method for Finding Saddle Points on High Dimensional Potential Surfaces Using Only First Derivatives. *J. Chem. Phys.* **1999**, *111*, 7010–7022.
- (28) Bader, R. F. W. A Quantum Theory of Molecular Structure and Its Applications. *Chem. Rev.* **1991**, *91*, 893–928.
- (29) Himpfel, F. J.; Christmann, K.; Heimann, P.; Eastman, D. E. Adsorbate Band Dispersions for C on Ru(0001). *Surf. Sci.* **1982**, *115*, L159–L164.
- (30) Köhler, L.; Kresse, G. Density Functional Study of CO on Rh(111). *Phys. Rev. B: Condens. Matter Mater. Phys.* **2004**, *70*, 165405.
- (31) Lichtenstein, L.; Heyde, M.; Freund, H.-J. Crystalline-Vitreous Interface in Two Dimensional Silica. *Phys. Rev. Lett.* **2012**, *109*, 106101.
- (32) Zhang, Z.; Yates, J. T. Band Bending in Semiconductors: Chemical and Physical Consequences at Surfaces and Interfaces. *Chem. Rev.* **2012**, *112*, 5520–51.
- (33) Kingdon, K. H.; Langmuir, I. Thermoionic Phenomena Due to Alkali Vapors. Part I, Experimental. *Phys. Rev.* **1923**, *21*, 380–381.
- (34) Gurney, R. W. Theory of Electrical Double Layers in Adsorbed Films. *Phys. Rev.* **1935**, *47*, 479–482.
- (35) Wertheim, G. K.; DiCenzo, S. B.; Youngquist, S. E. Unit Charge on Supported Gold Clusters in Photoemission Final State. *Phys. Rev. Lett.* **1983**, *51*, 2310–2313.
- (36) Bagus, P. S.; Wieckowski, A.; Freund, H.-J. The Contribution of Lattice Strain to Core-Level Binding Energy Shifts in Metal Nanoparticles: Generality and Origin of the Shifts. *Comput. Theor. Chem.* **2011**, *987*, 22–24.
- (37) Sinha, S.; Badrinarayanan, S.; Sinha, A. P. B. The Pd-H System Revisited: An XPS and UPS Study. *J. Phys. F: Met. Phys.* **1986**, *16*, L229–L232.
- (38) Moulder, J. F.; Stickle, W. F.; Sobol, P. E.; Bomben, K. D. *Handbook of X-Ray Photoelectron Spectroscopy*; Perkin-Elmer Corporation: Eden Prairie, MN, 1992.
- (39) Kaden, W. E.; Kunkel, W. A.; Roberts, F. S.; Kane, M.; Anderson, S. L. CO Adsorption and Desorption on Size-Selected Pd(n)/TiO₂(110) Model Catalysts: Size Dependence of Binding Sites and Energies, and Support-Mediated Adsorption. *J. Chem. Phys.* **2012**, *136*, 204705.
- (40) Andersen, J. N.; Hennig, D.; Lundgren, E.; Methfessel, M.; Nyholm, R.; Scheffler, M. Surface Core-Level Shifts of Some 4d-Metal Single-Crystal Surfaces: Experiments and Ab-Initio Calculations. *Phys. Rev. B* **1994**, *50*, 17525–17534.
- (41) Citrin, P. H.; Wertheim, G. K. Core-Level Binding Energy and Density of States from the Surface of Atoms of Gold. *Phys. Rev. Lett.* **1978**, *41*, 1425–1428.
- (42) Wagner, C. D. A New Approach to Identifying Chemical States, Comprising Combined Use of Auger and Photoelectron Lines. *J. Electron Spectrosc. Relat. Phenom.* **1977**, *10*, 305–315.

(43) Hohlneicher, G.; Pulm, H.; Freund, H.-J. On the Separation of Initial and Final State Effects in Photoelectron Spectroscopy Using an Extension of the Auger-Parameter Concept. *J. Electron Spectrosc. Relat. Phenom.* **1985**, *37*, 209–224.

(44) Kaden, W. E.; Büchner, C.; Lichtenstein, L.; Stuckenholtz, S.; Ringleb, F.; Heyde, M.; Sterrer, M.; Freund, H.-J.; Giordano, L.; Pacchioni, G.; Nelin, C. J.; Bagus, P. S. Understanding Surface Core-Level Shifts Using the Auger Parameter; a Study of Pd Atoms Adsorbed on SiO₂ Ultra-Thin Films. *Phys. Rev. B* **2014**, *89*, 115436–115443.

(45) Bagus, P. S.; Brundle, C. R.; Pacchioni, G.; Parmigiani, F. Mechanisms Responsible for the Shifts of Core-Level Binding Energies Between Surface and Bulk Atoms of Metals. *Surf. Sci. Rep.* **1993**, *19*, 265–283.